High Proton Conductivity of a Bismuth Phosphonate Metal–Organic Framework with Unusual Topology

Pablo Salcedo-Abraira, Catalina Biglione, Sérgio Vilela, Erik Svensson Grape, Nieves Ureña, Fabrice Salles, María Teresa Pérez-Prior, Tom Willhammar, Philippe Trens, Alejandro Várez, et al.

High Proton Conductivity of a Bismuth Phosphonate Metal-Organic Framework with Unusual Topology

Pablo Salcedo-Abraira,[a†] Catalina Biglione,[a] Sérgio M. F. Vilela,[a] Erik Svensson Grape,[b] Nieves Ureña,[c] Fabrice Salles,[d] María Teresa Pérez Prior,[c] Tom Willhammar,[b] Philippe Trens,[d] Alejandro Várez,[c] A. Ken Inge,[b*] Patricia Horcajada [a*]*

a. Advanced Porous Materials Unit, IMDEA Energy Institute, Avda. Ramón de la Sagra 3, Móstoles 28935, Madrid, Spain.

b. Department of Materials and Environmental Chemistry, Stockholm University, Stockholm 106 91, Sweden.

c. Department of Materials Science and Engineering and Chemical Engineering, IAAB, Universidad Carlos III de Madrid, Avda. Universidad 30, Leganés 28911, Madrid, Spain.

d. ICGM, Univ. Montpellier, CNRS, ENSCM, Montpellier 34095, France

TOC graph:

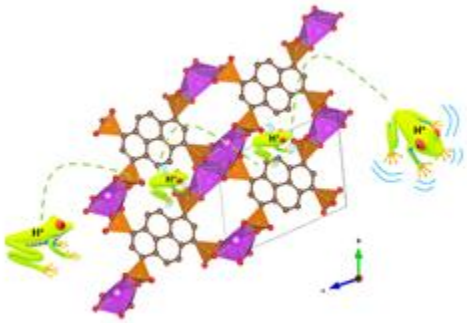

ABSTRACT

Despite the interest of proton exchange membrane (PEM) technologies (fuel cells, electrolyzers) for energy applications, the low stability of the electrolyte materials under working conditions (i.e. humidity and temperature) is one of their major limitations. Metal-Organic Frameworks (MOFs) have recently emerged as promising electrolytes due to their higher stability compared with the currently applied organic polymers, proton conductivity and outstanding porosity. Here, a novel robust Bi phosphonate MOF (branded as IEF-7) was successfully synthesized and fully characterized, exhibiting a completely new topology based on an unusual Bi coordination. Further, IEF-7 exhibited potential porosity, very high chemical and thermal stability, and free $–PO_3H$ groups involved in its ultra-high proton conductivity, reaching $1.39 \cdot 10^{-2}$ $S \cdot cm^{-1}$ at 90 °C and 90 % relative humidity for, at least, 3 cycles. In order to improve the consolidation and shaping of the powder for testing its ion conductivity properties, a highly MOF loaded composite (90 wt.%) was prepared by adding a proton conductive sulfonated polysulfone-binder. The degree of sulfonation of the binder was optimized to obtain the best compromise between proton conductivity and mechanical consistency of the pellet. The proton conductivity of the resulting composite was in the same order of magnitude as the compacted MOF powder, making this polymeric composite electrolyte very promising for PEM technologies.

1. INTRODUCTION

With an exceptional regular porosity, and enormous chemical and topological versatility,[1–4] Metal-Organic Frameworks (MOFs) have been proposed in a wide variety of strategic applications (fluid separation and storage[5–7], catalysis[8–10], environment[11–13], energy[14–17] and biomedicine[18–20]). However, a restricted chemical stability is often considered a limitation for real application.[21,22] According to the hard and soft acids and bases (HSAB) principle[23]; hard metals, e.g. tetravalent M(IV) and trivalent cations M(III) form stable bonds with hard polycomplexing ligands (e.g. carboxylates, phosphonates), while soft metals, e.g. divalent cations M(II), form stable bonds with soft polycomplexing ligands (e.g. nitrogenated) leading to robust materials. Despite their frequent instability, most of reported MOF structures are based on M(II) and carboxylate linkers. In particular, phosphonate-based MOFs (or P-MOFs) are much less explored than carboxylate MOFs (P-MOFs vs. carboxylate-MOFs ≈ 1:10; according to Web of Science, Feb. 2023). This could be explained by the poor solubility of the phosphonate linkers and their low commercial availability, as well as by the challenging elucidation of their crystal structures, limiting the number of currently available P-MOFs. Nevertheless, P-MOFs are attracting a growing interest since phosphonate ligands can lead to robust MOFs with a high versatility in the coordination modes (i.e. different protonation states) and multiple non-covalent interactions.[24,25]

Further, P-MOFs have recently emerged as excellent proton conductive materials with potential as proton exchange membranes (PEMs), which are currently used in proton exchange membrane fuel cells (PEMFCs)[26–28] and electrolyzers[29–31]. These devices

are of great relevance considering the growing environmental issues associated with the emission of greenhouse gases caused by conventional fuels.

Even though some MOFs have already demonstrated ultra-high proton conductivity (up to 10^{-1} S·cm^{-1})[32,33], there are only few reports where the MOF stability is assessed under relevant conditions (high temperatures and relative humidity values).[34–37] Meanwhile, P-MOFs could not only present good proton conductivity (associated with a larger number of labile protons when compared to sulfonate- or carboxylate-MOFs), but also high stability, resulting from their often stronger coordination than carboxylate and N-donor MOFs.[24,38] In this matter, the MOF community has recently reported highly stable porous MOFs employing phosphonate and high valency metals (*e.g.* Hf, Zr). [39–45] Among them, only 3 structures have been evaluated in proton conductivity reaching low to good values (10^{-4} to 10^{-2} S cm^{-1}).[42,46–48]

In this context, we report here a novel Bi(III) pyrene tetraphosphonate P-MOF, branded as IEF-7 (IEF stands from IMDEA Energy Framework), showing Bi(III) in an unusual coordination environment. One should highlight that, despite the huge number of topologies described in MOFs,[49] the underlying net of IEF-7 has not been previously reported. All eight Bi-phosphonate coordination polymers reported so far consist of the coordination of halides to Bi(III), while IEF-7 is the first example lacking the presence of halides.[50] Furthermore, this material presents great thermal (up to 400 ºC) and chemical (in several organic solvents and wide range of pH) stability. Finally, the proton conductivity of IEF-7 as well as its polymer-based composite was here investigated, being a pioneer study on Bi P-MOFs, evaluating the conductivity and cyclability as a function of temperature and relative humidity (RH) obtaining encouraging preliminary results.

2. MATERIAL AND METHODS

Reagents. All the reagents were used as received without any purification: Bismuth (III) nitrate pentahydrate ($Bi(NO_3)_3 \cdot 5H_2O$ 98%, Acros Organics);; pyrene ($C_{16}H_{10}$, 98%, Sigma Aldrich); nitrobenzene ($C_6H_5NO_2$, 99%, Thermo Scientific); bromine (Br_2, ≥95,5%, Sigma Aldrich); tetrakis(triphenylphosphine)palladium(0) ($[Pd(PPh_3)_4]$, 99%, Sigma Aldrich); triethyl phosphite ($P(OC_2H_5)_3$, 98%, Sigma Aldrich); Udel® Polysulfone, petroleum ether (C_6H_{14}, ≥95%, LabKem); *n*-hexane (C_6H_{14}, technical grade, VWR Chemicals); hydrochloric acid (HCl, 37-38 %, J.T. Baker); dichloromethane (CH_2Cl_2, 96 %, VWR Chemicals); methanol (CH_3OH, ≥99,9%, Chem-Lab); tetrahydrofuran (C_4H_8O, ≥99,9%, Chem-Lab); acetonitrile (C_2H_3N, ≥99,5%, Honeywell); N,N-dimethylformamide (C_3H_7NO, ≥99,5 %, Chem-Lab); octane (C_8H_{18}, ≥98%, Alfa Aesar); toluene (C_7H_8, 99,8%, LabKem)

2.1 Synthetic Procedure

2.1.1 Bulk IEF-7 $Bi_2(Py(PO_3)_2(PO_3H)_2)$: 899.31 mg (1.854 mmol) of $Bi(NO_3)_3 \cdot 5H_2O$ and 484.05 mg (0.927 mmol) of the lab-made linker $Py(PO_3H_2)$ (see ESI, Scheme 1) were dispersed in 61.8 mL of a mixture of distilled H_2O, MeOH and 6M HCl (volumetric ratio 0.45:1:0.05) inside a 103 mL Teflon-lined autoclave. Then, the reactor was closed and heated from room temperature (RT) to 120 °C in 6 h, maintaining this temperature for 48 h. After cooling to RT for 6 h, the obtained brown material was filtered and washed with water and methanol, recovered and dried under air. Yield: 60%. See patent P201931095 for further information.[51]

2.1.2 Higher Crystallinity IEF-7 $Bi_2(Py(PO_3)_2(PO_3H)_2)$ (used to solve the structure by 3DED): 26.536 mg (0.045 mmol) of BiI_3 and 11.749 mg (0.023 mmol) of the lab-made

linker Py(PO_3H_2) (see ESI) were dispersed in a 1.5 mL of a mixture of distilled H_2O, MeOH, 6M HCl and formic acid (volumetric ratio 0.366:1:0.05:0.084) inside a 2.5 mL Teflon-lined autoclave. Then, the reactor was closed and heated from RT to 120 °C in 6 h, keeping this temperature for 48 h. After cooling to RT in 6 h, the obtained brown material was filtered and washed with water and methanol, recovered and dried under air.

2.1.3 Sulfonated Polysulfone (SPSU): SPSU was synthesized according to a previous report (Scheme S2).[52] 5 g of polysulfone (Udel®, PSU, 22000 g mol^{-1}) was dissolved in 30 mL of 1,2-dichloroethane (DCE) under inert atmosphere at ambient temperature. After the polymer dissolution, the sulfonating agent (trimethylsilyl chlorosulfonate, or TMSCS; previously dissolved in DCE with a 1:1 PSU:TMSCS molar ratio) was added dropwise and maintained during 24 h. A sulfonation reaction of PSU was performed using TMSCS since lower degradation of polymer chains was reported in a previous study.[53] The resulting polymer was precipitated in a 0.1 M solution of sodium hydroxide, and dried under vacuum at 60 °C.

2.2 Crystallographic Studies

Three-dimensional electron diffraction (3DED) data were collected using a JEOL JEM2100 TEM, equipped with a Timepix detector from Amsterdam Scientific Instruments, while continuously rotating the crystal at 0.45° s^{-1}. The experiment was carried out through the aid of Instamatic,[54] with data reduction performed in XDS.[55] A total of six crystals were used for the data collection, for which the individual data were merged. The acquired intensities were then used to solve the structure with SHELXT,[56] and refined using SHELXL,[57] with electron scattering factors which were extracted from SIR2014.[58]

The topological analysis of the framework was carried out using the software package ToposPro,[59] as well as Systre,[60] and 3dt (both part of the GAVROG package).[61] Powder X-ray diffraction (PXRD) data were collected in an Empyrean Panalytical diffractometer (Cu Kα, λ =1.5406 Å), equipped with a PIXcel3D detector, operating at 45 kV and 40 mA with 0.02 rad soller slits from 3 to 90 2θ° with an acquisition time of 120 s and refined by FullProf.[62]

2.3 Molecular Simulation

In order to propose a plausible structure, a geometry optimization was performed using Forcite with partial charges calculated from the electronegativity equalization method combined with UFF parameters[63] to calculate the electrostatic part and the van der Waals interactions. The electrostatic interactions were calculated by Ewald summation, while the short-range contributions corresponding to Lennard Jones parameters were computed by applying the Lorentz-Berthelot rules. The simulations were conducted using a multicell (corresponding to 7x3x3 unit cells), which is consistent with a cut-off distance for Lennard Jones interactions equal to 12.5 Å. Equilibration and production were achieved after 5 million steps at 298 K. The energy criteria was used to determine the plausible theoretical structure.

The accessible surface area and pore volume of the simulated structure was estimated using the strategy previously reported by Düren *et al*.[64] This surface was calculated from the center of a nitrogen probe molecule rolling across the surface. While the radius of the nitrogen probe molecule was considered to be 1.835 Å, the diameters of each atom constituting the IEF-7 structure were taken from the UFF force field.[63]

The free volume was calculated by using a similar method of trial insertions within the entire volume of the unit cell. A probe size of 0 Å was used to enable us to determine this total free volume of the unit cell that is not occupied by the atoms of the framework.[64] Finally, using the same parametrization for the framework (UFF), the methodology of Gelb and Gubbins[65] was used to calculate the pore size distribution (PSD), in order to estimate the pore size or cavity size.

In order to investigate the conductive pathways and the organization of the water molecules inside the IEF-7 pores, Monte Carlo simulations (using SORPTION (available in Materials Studio) have been performed using the same force field than previously. In this case, the mobile H^+ have been considered. For these calculations, equilibration and production were achieved after 200 million and 100 million steps at 298 K.

2.4 Characterization

Scanning electron microscopy (SEM) micrographs were collected on a Hitachi TM-1000 microscope operating at 15 kV. PXRD routine patterns were collected in an Empyrean Panalytical diffractometer (Cu Kα, λ =1.5406 Å) equipped with a PIXcel3D detector and operating at 45 kV and 40 mA. Fourier transform infrared (FTIR) spectra were collected using a Thermo Nicolet 6700 FTIR with ATR accessory instrument in the 4000 to 400 cm^{-1} range (Thermo scientific, USA). Light elements (C, H, N, S) analyses were carried out in a Flash 2000 analyzer from Thermo Scientific. Inductively coupled plasma optical emission spectroscopy (ICP-OES) measurements (Bi, P) were done in a 2300 DV spectrometer equipment from Perkin Elmer. Thermogravimetric analyses (TGA) were performed using a SDT Q-600 thermobalance (TA instruments) in the 25–800 °C range under at 5 $°C \cdot min^{-1}$ and an air flow of 100 $mL \cdot min^{-1}$. TG-VSA were carried out employing a STA 449 F3

Jupiter, equipped with a water-vapor furnace. The experiment was performed with a ramp of 3 ºC·min^{-1} from 105 ºC to until 200 ºC, where the temperature was maintained for 30 min and then, cooled-down to 125 ºC (3 ºC·min^{-1}). Then, the water vapor (90 % RH) was introduced for 30 min. This cycle was repeated 4 times. Finally, a heating ramp of 3 ºC·min^{-1} was set to finally reach 800 ºC. The TGA of the membranes was performed in a Pyris TGA1 instrument from Perkin-Elmer under air atmosphere at a rate of 10 °C min^{-1} heating from 40 to 600 °C.Variable temperature PXRD (VTPXRD) data were acquired on a D8 Advance Bruker AXS θ–2θ diffractometer (Cu Kα X-radiation, λ=1.54060 Å), equipped with an Anton Paar XRK 900 high-temperature chamber and a LYNXEYE XE detector, operating at 40 kV and 40 mA. Nitrogen sorption isotherms were performed at 77 K using a Quantachrome iQ3 Autosorb. Prior to the analysis the samples were activated at 300 °C under primary vacuum during 5 h. Proton nuclear magnetic resonance spectroscopy (^{1}H-NMR) spectra were adquired on a Bruker Avance DPX-300 spectrometer at 300 MHz using N,N'-dimethylformamide (DMF-d_7) and dimethyl sulfoxide (DMSO-d_6) as the solvents. TMS was used as the internal reference.

Water sorption experiments were also performed in order to determine the water sorption capacity at high RH, but also to evaluate the water / IEF-7 affinity through the Henry's constant at low coverage. For this purpose, the material was degassed at 150°C under secondary vacuum (better than 10^{-5} torr) for 24 h. Deionised water was degassed under vacuum for removing dissolved gases before sorption experiments. The water sorption isotherm was determined at 25°C using a home-made device, based on manometric measurements (with two capacitive pressure gauges (0-10 Torr and 0-1000 Torr)). This device allows for setting increasing pressure pulses, instead of setting equilibrium

pressures. 120 s was chosen as thermodynamic stability criterion for each data recorded, considering a pressure variation lower 0.0025 Torr during this time period. To assess this equilibration criterion, we measured a second sorption isotherm with a longer time of equilibrium (180s), leading to the same sorption isotherm. The whole water sorption isotherm was completed in 28h.

2.5 Proton Conductivity Measurements

The proton conductivity (σ) of the materials was investigated by impedance spectroscopy (IS). Compacted pellets of crystalline IEF-7 or SPSU composites were prepared by applying uniaxial pressure (49 MPa; ~6 mm diameter). The faces of the pellets were coated by Au ion-blocking electrodes by sputtering in a Leica EM ACE 200 instrument. The electrical measurements were carried out on a parallel-plate capacitor configuration under air. Measurements were performed using an impedance/gain-Phase analyzer SI 1260 (Solartron, UK), applying a 100 mV amplitude signal in the 10^{-1}-10^{7} Hz frequency range. Measurements at different relative humidity (70-90% RH) and temperatures (30-90 °C) were performed in a programmable climatic oven (BINDER, UK). In order to ensure the reproducibility, the samples were dried overnight at 60 °C before starting the measurements. A dwell time of 15 min and 1 h was defined to allow the system to reach stable temperature and humidity conditions, respectively. By using this procedure, the RH and temperature can be controlled up to ±1% and ±1 °C, respectively.

The impedance data analysis was performed using the ZView2 program.[66] The σ (in S cm^{-1}) was calculated by the following equation:

$$\sigma = \frac{l}{R \, X \, A} \qquad (1)$$

where l and A are the thickness (cm) and the area (cm^2) of the pellets, respectively. R is the ohmic resistance (Ohm) obtained from the intersection of the high frequency arc the axis of the real component of the impedance plot. Finally, the pseudo-activation energy is calculated according to the following equation,

$$\sigma = \sigma_o * exp\left(\frac{-E_a^{VTF})}{K(T-T_0)}\right), \quad (2)$$

where σ_0 is the preexponential factor, T is the absolute temperature, K is the Boltzmann constant, $E_a{}^{VFT}$ is the pseudo-activation energy, and finally T_0, when considering polymers, is the glass transition temperature at which the "free" volume disappears or at which the configuration free entropy becomes zero. In this case, T_0 could also be related to the temperature at which molecular water motions cease.

3. RESULTS AND DISCUSSION

3.1 Synthesis and crystal structure of IEF-7

A novel MOF, denoted IEF-7, was synthesized from bismuth and the lab-made pyrene tetraphosphonic acid ($Py(PO_3H_2)_4$) (easily prepared at multi-gram scale, see supporting information, SI), after optimizing the synthesis conditions (solvents, Bi precursor, time, temperature, etc.) by using the efficient high-throughput method.[67] Briefly, IEF-7 was obtained by solvothermal-heating of a mixture of $Py(PO_3H_2)_4$ and $Bi(NO_3)_3{\cdot}5H_2O$ in a mixture of water/methanol/hydrochloric acid at 120 °C for 60 h, reaching yields of 60% (based on the initial metal). Interestingly, during the synthetic optimization process, it was observed that both bismuth concentration and linker-to-metal ratio (L/M) have a strong influence on the purity of the resulting material. When the amount of bismuth is higher (either increasing its concentration or reducing the L/M ratio) additional peaks (impurity)

appear in the powder X-ray diffraction (PXRD) patterns (see Figures S1 and S2). The same crystalline impurity was also present when changing the Bi source (when BiOCl was used instead $Bi(NO_3)_3 \cdot 5\ H_2O$ or BiI_3, Figure S3). In contrast, the temperature has a poor influence on the nature of the final material, always obtaining the IEF-7 phase within the 100 – 140 °C range and only observing a small impurity when synthesized at lower temperature (80 °C, Figure S4). Note here the successful scale-up of the synthesis from 1.5 to 61.8 mL, producing up to 500 mg in a single reaction. In all cases, small elongated crystals were isolated (around 0.5-1 μm, Figure S5), preventing their structural unveiling by conventional single crystal X-ray diffraction. The crystalline structure of IEF-7 (Figure 1) was thus elucidated from a *ca.* 1 μm single crystal (Figure S6) by 3D electron diffraction (3DED), a powerful and proven method for solving the structure of microcrystalline materials.[68] Specifically, the structures for many of the published bismuth-based MOFs have been elucidated using 3DED as they are often obtained as microcrystalline products.[68] . IEF-7, with molecular formula $[Bi_2Py(PO_3)_2(PO_3H)_2]$ (MW = 934.08), crystalizes in the space group nº2 (triclinic, *P*-1) (Table S1, CCDC 2161748).

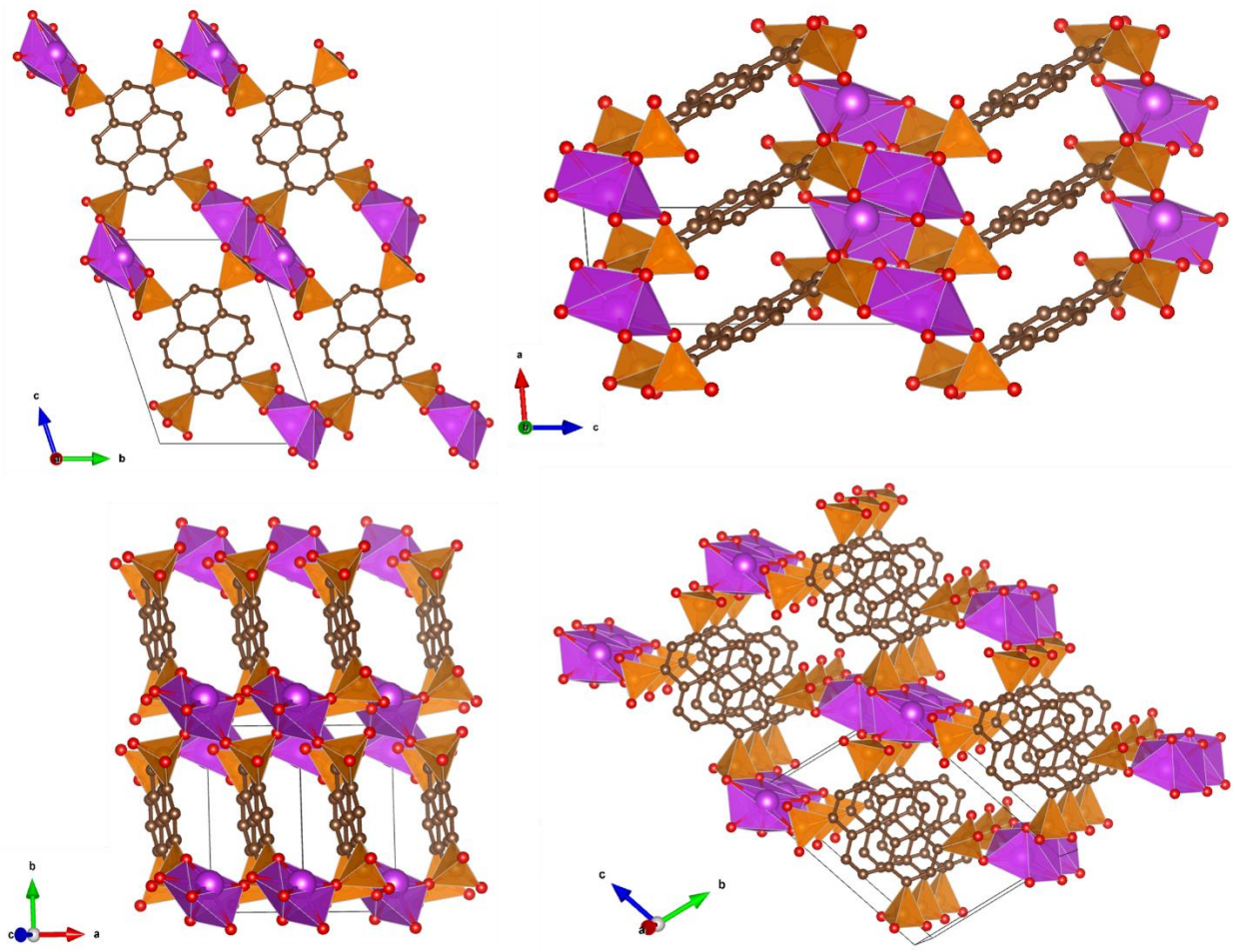

Figure 1. Crystalline structure views along different axes of the IEF-7. Bi, P, C and O are represented in purple, orange, brown and red, respectively. Hydrogen atoms were removed for clarity.

The structure is built up from Bi_2O_{10} clusters as SBUs (Figure S7). Each Bi is coordinated to six O in a distorted pentagonal pyramidal geometry, with the Bi atom located in the base of the pyramid rather than the center. This coordination geometry could be justified considering the stereochemically active lone pair effect typical of the group 15 elements, as supported by the Bi-O distance found between the Bi and the axial O, which is shorter than the equatorial ones (*ca.* 2.2 *vs.* 2.5 Å, Figure S8). The O6, O2 and O3 are in the same

plane as Bi, meanwhile the other two oxygens are out of the plane forming a 113.7º angle with the Bi. The two pyramids in the SBU share an edge and are related to one another by inversion symmetry. Each SBU is connected to five different phosphonate linkers. The pyrene-based linker also has inversion symmetry. Two of the four phosphonate groups are coordinated to two Bi cations through two monodentate O atoms, which leaves one of the O atoms on the phosphonate group not involved in coordination to Bi. The other two phosphonate groups coordinate to three Bi cations through all three O atoms which are fully deprotonated and are both mono- and bidentate. Figure 2 shows a topological representation of the IEF-7 structure, with a trinodal 3,3,5-c net with a transitivity of 3784 (3 kinds of vertices, 7 kinds of edges, 8 kinds of faces, 4 kinds of tiles), disclosing two types of potential pores (see the pink and purple ellipsoids). Remarkably, this unusual topology has not been described in the literature. In order to maintain electro-neutrality, one of the phosphonate groups of the asymmetric unit (*i.e.* two *per* linker) is expected to be protonated. According to the distances found in the phosphonic group having only two O coordinated to the Bi (P1-O1, P1-O2 and P1-O3; 1.626, 1.599 and 1.541 Å, respectively), we hypothesized that the hydrogen might interact with the O1. It was then possible to propose a plausible crystal structure by performing a geometry-optimization using Forcite and classical force fields (UFF) starting from the experimental result obtained by 3DED.

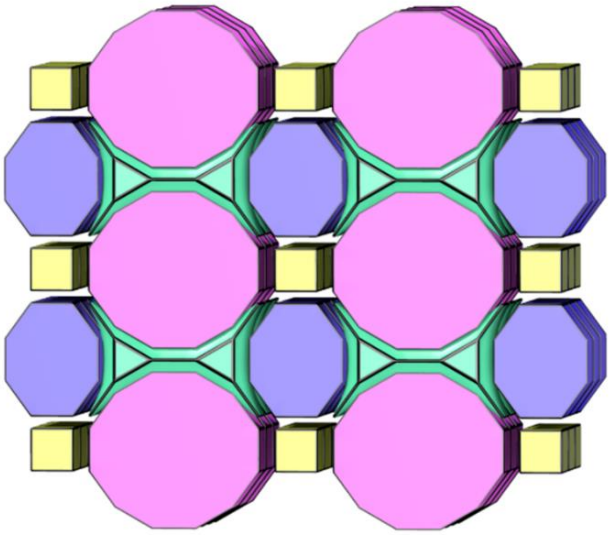

Figure 2. Topological representation of the IEF-7 structure. In green is represented the ligand, yellow the metal, pink the large pores and purple the smaller ones.

The plausible structure, given in the Supplementary Information (SI) and presented in Figure S9, shows clearly Bi-O distances close to 2.259 Å and P-O ranging from 1.731 (for the OH) to 1.750-1.781 Å (for the others). In addition, C-P distances are close to 1.913 Å. Further, the distances for the H^+ with the phosphate groups can also be evaluated by considering the proton as mobile and using Monte Carlo simulations. It can therefore be shown that the H^+ moves from one phosphate group to the other (see Figure S10) with distances ranging between 2.13 Å to 3.3 Å and jumping from one P-O bond to another one. Such a structure will be useful to explain the conductivity measurements mainly governed by the ability of the protons to move in a very constrained porosity.

From the crystalline structure, potential voids (~3.5x4 Å) are present. However, only a small nitrogen sorption capacity was measured at 77K (Figure S11), leading to a rather moderate specific surface area of ~ 34 $m^2 \cdot g^{-1}$, as determined using the BET (Brunauer-Emmett-Teller) transform of

the sorption isotherm. This result can be explained considering the kinetic diameter of nitrogen molecules, which is close to the pore dimensions (3.64 Å).

3.2 Physicochemical characterization

The purity of the polycrystalline powder was confirmed by Le Bail refinement (Figure S12), which found lattice parameters by PXRD slightly different to those obtained by 3DED (Table S2). Such differences are rather common in part due to the fact that 3DED and PXRD experiments are carried out under vacuum and air, respectively, which could affect the unit cell parameters.

Fourier transform infrared (FTIR) spectra show a significant shift of the phosphonate bands in IEF-7 when compared to the free linker (from 1090 to 1082 cm^{-1} and from 1019 to1005 cm^{-1}; Figure S13), supporting the coordination of the phosphonate groups to bismuth. Also, the vibrational stretching band OH can be observed sharper at 3600 cm^{-1} in the IEF-7, in agreement with the presence of the free hydroxyl groups coming from the uncoordinated phosphonic acid of the linker.

The chemical composition of the IEF-7, $Bi_2(Py(PO_3)_2(PO_3H)_2)$, was confirmed by elemental analysis (C, H), inductively coupled plasma (ICP; P, Bi), and attributing the remaining atoms to oxygen: Theo. (%): C 20.57; H 0.86; O 20.55; P 13.3; Bi 44.7. Exp. (%): C 20.43; H 1.13; O 23.94; P 13.3; Bi 41.2. In addition, thermogravimetric analysis (TGA) shows a slight weight loss (1.8%, Figure S14) from room temperature (RT) to 200 °C, associated with the departure of water molecules. Then, at around 400 °C, the material starts to degrade, with the decomposition of the ligand until the formation of $Bi_2P_4O_{13}$ residue at 800 °C. The structural thermal stability was more precisely evaluated by VTPXRD. Remarkably, the IEF-7 structure was highly stable, with no structural significant

changes in the VTPXRD patterns up to 400 °C (in good agreement with the TGA data), leading to the crystalline $Bi_2P_4O_{13}$ phase after the decomposition of the linker (Figure S15). Further, to assess the chemical robustness of the material, powdered IEF-7 was suspended in aqueous solutions at different pH and in different organic solvents (see ESI for further details). Its structural integrity was evaluated by PXRD, and the degradation quantified by the ligand leaching to the solution using UV-Vis spectroscopy. It is interesting to note that IEF-7 not only presents a very high stability in all tested organic solvents (*i.e.* hexane, dichloromethane, acetonitrile, *N,N'*-dimethylformamide, dimethyl sulfoxide, and isopropanol; Figure S16), but also in aqueous solution. It is also important to highlight that the crystalline structure of IEF-7 was kept intact in a very broad pH range (pH = 1-10.5), with a degradation lower than 2% upon 16 h contact (Figure S17). The mechanical stability was also evaluated by pelletizing the material under uniaxial pressure (49 MPa). PXRD patterns from the resulting pellets were collected and compared with the pristine sample (Figure S18), confirming the IEF-7 structural integrity.

3.3 Proton conductivity of IEF-7

The presence of labile protons in the structure, in addition to its robustness, make IEF-7 an excellent proton conductive candidate. The proton conductivity (σ) of the pellets was determined by impedance spectroscopy (IS) at different experimental conditions (from 30 to 90 °C at RH = 70 and 90%; see experimental section for further details).

Typical impedance datasets of compacted powder of IEF-7 are displayed in Figure 3 and S19.

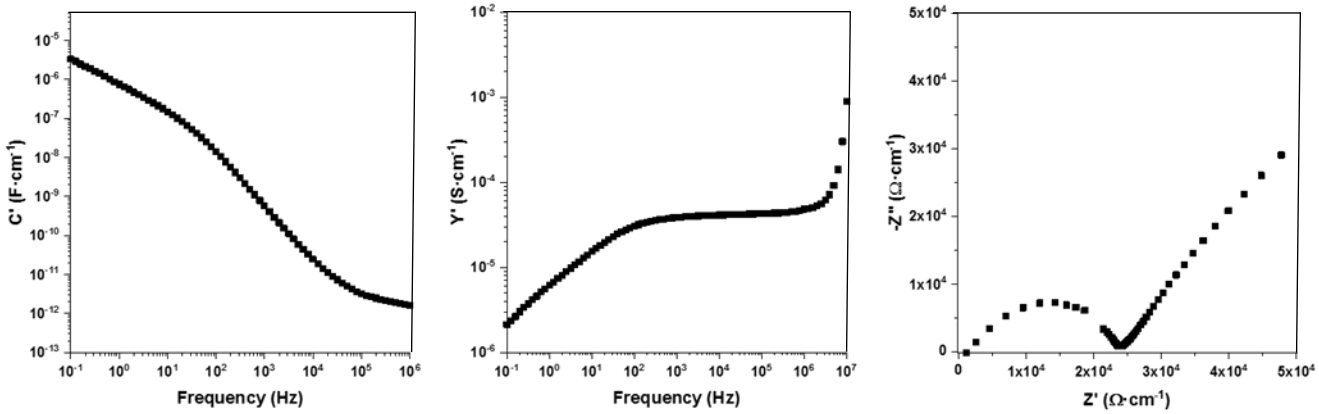

Figure 3. Impedance dataset of IEF-7 at 70% RH and 90 ºC.

The data show a slightly distorted semicircle with an associated capacitance (C) of 1.8 $pF \cdot cm^{-1}$ at high frequency, which can be attributed to the bulk resistance of the sample. At the low frequency region can be observed an inclined spike ($C = 3.3\ \mu F \cdot cm^{-1}$), indicating a partial-blocking electrode response (which is consistent with proton migration). Two different regions in the admittance plot can be differentiated: a plateau at high frequencies and dispersion at low frequencies. The plateau corresponds to constant conductivity associated with the bulk conductivity of the sample, in agreement with the resistance value extracted from the Nyquist plot.

Furthermore, the conductivity was measured at different RH (1%-90%) (Figure S20). It is noteworthy that the conductivity value increases by around 4 orders of magnitude with the humidity, which evidences the strong influence of the RH on the conductivity properties. For instance, the conductivity increases more than two orders of magnitude when the RH varied from 70 to 90% at 90 °C from $4.19 \cdot 10^{-5}$ to $1.39 \cdot 10^{-2}\ S \cdot cm^{-1}$ (Figure 4 and S29). Note here that this value is among the highest reported ones for MOFs (Table S3) and similar to

the benchmarked Nafion®. Despite the differences with the best reported proton conductive MOFs (*i.e.* 1K_Eu, Co-tri and BUT-8-(Cr) with $1.9 \cdot 10^{-1}$, $1.5 \cdot 10^{-1}$ and $1.3 \cdot 10^{-1}$ $S \cdot cm^{-1}$, respectively),[76–78] IEF-7 advantageously present a non-toxic composition (Bi *vs.* Eu, Co, Cr) and a lower price ($EuCl_3 \cdot 6H_2O$ 20k€$\cdot kg^{-1}$; $CoCl_2 \cdot 6H_2O$ 650€$\cdot kg^{-1}$; $Bi(NO_3)_3 \cdot 5H_2O$ 180€$\cdot kg^{-1}$; Prices extracted from Merck, www.merckmillipore.com) .

With the aim to shed some light on the proton conduction mechanism, the activation energy of the process was estimated. As depicted in Figure 4, the materials did not follow an Arrhenius behavior. In this context, pseudo-activation energies (E_a^{VTF}) were calculated by fitting the data using the Vogel-Tamman-Fulcher (VTF) model (Figure S21),[69] an extended approximation for non-Arrhenius polymeric ion conductors.[70] Although not completely understood yet, this non-Arrhenius behavior has been already described for other proton conducting MOFs materials.[71,72]

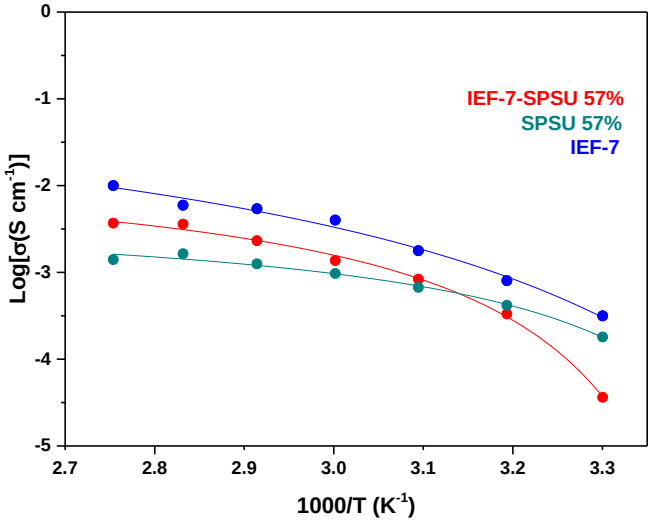

Figure 4. Arrhenius plots of pure IEF-7, IEF-7-SPSU 57% composite and pure SPSU 57% polymer at 90 % RH.

The values of the E_a^{VTF} obtained from the fitting (<0.5 eV, Table S4) corresponds to a Grotthuss mechanism,[73] which means that the proton mobility occurs through H-bonding from one carrier to another,[71,74] as also suggested by TGA experiments (TGA and TG VSA), water sorption isotherms and molecular simulation. In this sense, the TGA of the previously hydrated IEF-7 solid (overnight at 90%RH and RT) shows a first weight loss (4.9 wt%) at 50 ºC associated to water physisorbed on the outer surface of the crystals, followed by a second progressive weight loss (1.5. wt%) from 50 to 150 ºC, which might correspond to the water molecules adsorbed within the pores (Figure S22). Water sorption isotherms (Figure S23) evidence the progressive adsorption of water in the porosity, reaching 1.3±1 wt% at high RH (e.g. 90-100%). Note here that, despite the low nitrogen sorption capacity showed by the material, the smaller kinetic diameter of the water molecules (3.64 *vs.* 2.65 Å, respectively) allow them to enter into the MOF porosity. The water content estimated from the sorption isotherm is in good agreement with the previous TGA data. It can be noted that the slope of the sorption isotherm at low pressure is rather high compared to hydrophobic systems which is the indication of an interaction between water molecules and the pores of IEF-7. This can be understood by the fact that water molecules are tightly confined in the micropores of the material as they have similar size.

Additionally, to prove the process cyclability, thermogravimetric vapor sorption analysis (TG-VSA) were conducted under similar conditions to the conductivity measurements setup (90%RH), showing that the water adsorption process (1.5 wt%) is completely reversible for at least 4 cycles (Figure S24). Further, molecular simulation studies considering the mobile H^+ in the structure, concludes that water molecules are preferentially located in the large pore (as illustrated by the density of states in the Figure

S25; see also the pink pore in Figure 2). These results suggest that only one kind of pores might be involved in the conductivity, which could explain the interesting values obtained experimentally

3.4 Proton Conductivity IEF-7-SPSU Composite

Additionally, as a proof of concept of the preparation of the first mechanically stable IEF-7 based composite, a proton conductor polymeric binder (10 wt.%) was added to the MOF prior to the shaping process. The SPSU was selected as a binder due to: i) its polymeric and hydrophilic nature; and ii) its high proton conductivity [75]. SPSU with 57% degree of sulfonation (DS) was tested. The sulfonation reaction of PSU was successfully confirmed by means of ^{1}H-nuclear magnetic resonance (NMR) spectroscopy (Figure S26). Comparing both PSU and SPSU ^{1}H-NMR spectra in the 6.40 ppm < δ < 8.40 ppm range (corresponding to the aromatic protons), the latter showed that the peak associated with the protons adjacent to the attached sulfonic groups ($H_{4'}$) was upshifted (δ = 7.71 ppm). [75] The degree of sulfonation was calculated by using Kopf equation, as described by Iojoiu *et al.*[52]. TGA of the SPSU polymer (Figure S27) shows a high thermal stability at temperatures up to 100 °C under air atmosphere. The weight loss showed at the beginning of the experiment is associated with the water removal, and not to the degradation of the polymer itself. [75]

The composites with 10 wt.% of SPSU 57% were obtained by mixing (milling) with the IEF-7, and subsequently, pelletizing. These composites were labelled as IEF-7-SPSU 57%. It was shown by PXRD that the IEF-7 crystalline structure was kept intact (Figure S28).

Figure 4 gathers evolution of the proton conductivity with the temperature for pristine materials (IEF-7 and SPSU 57%) as well as the composite (IEF-7-SPSU 57%). Compared with IEF-7, a similar electrochemical behavior was observed for the IEF-7-SPSU

composite. As expected, the conductivity IEF-7-SPSU 57% strongly depends on the temperature and RH (Figure 4 and S30), increasing more than two orders of magnitude when the RH varied from 70 to 90% at 90 °C (from $3.47 \cdot 10^{-5}$ to $3.69 \cdot 10^{-3}$ for IEF-7-SPSU 57%). The change of the E_a (Table S4) from the IEF-7 to the IEF-7-SPSU 57% indicates a contribution of the SPSU on the proton conductivity, with slightly lower activation energy in the composites than pristine MOF. Interestingly, the sample with the SPSU 57% binder showed close proton conductivity values than pure IEF-7, and improve the shaping of IEF-7. This fact favors the potential shaping of MOFs powders in similar operating cells than those of PEM fuel cells

3.5 Cyclability

The proton conductivity performance of IEF-7 was maintained for at least 3 cycles (Figure 5). Furthermore, the structural and chemical stabilities were proved by PXRD and FTIR analysis (Figures S31-32).

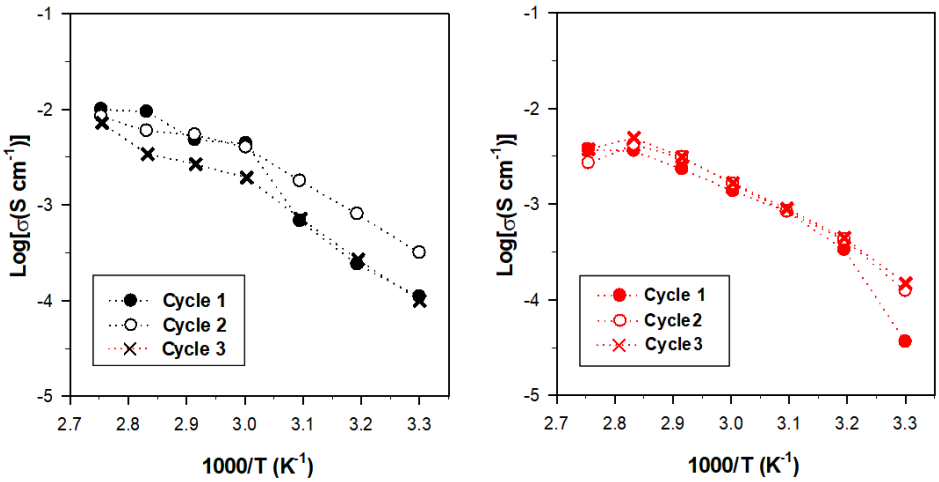

Figure 5. Cyclability Arrhenius plots of pure IEF-7 (right) and IEF-7-SPSU 57 % composite (left).

In the case of the IEF-7-SPSU 57% composite, the proton conductivity and crystalline structure were maintained (Figure 5 and S33). Furthermore, the consistency remained intact in the entire temperature range. These preliminary results demonstrate the potential of IEF-7 for its incorporation into polymeric membranes of different nature, being possible to combine high mechanical stability and proton conductivity. This fact paves the way to the incorporation in the near future in a proton exchange membrane device and the evaluation of its potential in real conditions.

4. CONCLUSION

A novel robust Bi-based P-MOF (branded as IEF-7) has been successfully synthesized. This solid exhibits an unusual topology based on Bi(III) in a non-common coordination environment (Bi_2O_{10} distributed into two distorted edge-sharing pentagonal pyramids), with an exceptional chemical and thermal robustness, even under very aggressive conditions. Associated with the presence of free $–PO_3H$ acidic groups and water, IEF-7 presents a high and cyclable proton conductivity (up to $1.39 \cdot 10^{-2}$ $S \cdot cm^{-1}$ at 90% RH and 90 °C). Also, the combination of IEF-7 with a sulfonated polysulfone polymer in a 10 wt.% favors the consolidation of the hybrid powders, enhancing the mechanical properties of the material. Therefore, the incorporation of the SPSU binder has proven to be an excellent strategy to improve the shaped MOFs while maintaining their transport properties, and lays the groundwork as a proof of concept of MOF polymer composites, highlighting the promising future of MOFs as electrolytes in fuel cell or electrolyzer devices.

ASSOCIATED CONTENT

Supporting information

Synthetic procedure of the ligand, scheme of SPSU, synthesis PXRD patterns, SEM micrography, crystallographic parameters, MOF structures, N_2 and water adsorption, Le Bail profile refinements, FTIR spectra, TGA and TG-VSA, TV-XRD experiments, chemical stability tests, impedance spectra, conductivities measurements, VTF fitting, molecular simulations, NMR and TGA characterization of SPSU, PXRD of pelletized IEF-7 and IEF-7-SPSU composites. Comparative table with ultra-high proton conductive MOFs.

AUTHOR INFORMATION

Corresponding authors

Patricia Horcajada – Advanced Porous Materials Unit, IMDEA Energy, Móstoles, Madrid, E-28935, Spain

E-mail: patricia.horcajada@imdea.org

Andrew Kentaro Inge – Department of Materials and Environmental Chemistry, Stockholm University, Stockholm 106 91, Sweden.

E-mail: andrew.inge@mmk.su.se

Alejandro Várez – Department of Materials Science and Engineering and Chemical Engineering, IAAB, Universidad Carlos III de Madrid, Avda. Universidad 30, E-28911 Leganés, Madrid, Spain.

E-mail: alvar@ing.uc3m.es

Present address

†**Pablo Salcedo-Abraira** – Nantes Université, CNRS, Institut des Matériaux de Nantes Jean Rouxel, IMN, F-44000 Nantes, France

Author Contributions

The manuscript was written through contributions of all authors. All authors have given approval to the final version of the manuscript.

ACKNOWLEDGMENT

Authors acknowledge the María de Maeztu IMDEA Energy Institute, Ramón Areces Foundation project H+MOFs, the M-ERA-NET C-MOF.cell project and Retos Investigación MOFSEIDON project (PID2019-104228RB-I00, MICIU-AEI/FEDER, UE). Authors also thank the Agencia Española de Investigación /Fondo Europeo de Desarrollo Regional (FEDER/UE) for funding the project PID2019-106662RBC43. This work has also been supported by Comunidad de Madrid (Spain) - multiannual agreement with UC3M ("Excelencia para el Profesorado Universitario" - EPUC3M04) - Fifth regional research plan 2016-2020. Support from the Swedish Foundation for Strategic Research (SSF) is also acknowledged. Dedicated to the fruitful and outstanding scientific career of Clément Sánchez, timelessly inspiring countless multidisciplinary researchers.

ABBREVIATIONS

Proton exchange membrane fuel cells, PEMFCs; Metal Organic Framework, MOF; phosphonate-based metal organic frameworks, P-MOF, IMDEA Energy Framework, IEF; relative humidity, RH; pyrene tetraphosphonic acid, $Py(PO_3H_2)_4$; powder X-ray diffraction, PXRD, 3D electron diffraction, 3DED; supporting information, SI; Fourier transform infrared, FTIR; inductively coupled plasma; ICP; room temperature, RT; thermogravimetric analysis, TGA; variable-

temperature powder X-ray diffraction, VTPXIRD; impedance spectroscopy, IS; activation energy, E_a; Vogel-Tamman-Fulcher, VTF; thermogravimetric vapor sorption analysis, TG VSA; sulfonated polysulfone, SPSU; degree of sulfonation, DS; polysulfone, PSU; nuclear magnetic resonance, NMR; water absorption capacity, WU%.

REFERENCES

[1] G. Ferey, A Chromium Terephthalate-Based Solid with Unusually Large Pore Volumes and Surface Area, Science (80-.). 309 (2005) 2040–2042. https://doi.org/10.1126/science.1116275.

[2] H. Furukawa, N. Ko, Y.B. Go, N. Aratani, S.B. Choi, E. Choi, A.O. Yazaydin, R.Q. Snurr, M. O'Keeffe, J. Kim, O.M. Yaghi, Ultrahigh Porosity in Metal-Organic Frameworks, Science (80-.). 329 (2010) 424–428. https://doi.org/10.1126/science.1192160.

[3] O.K. Farha, I. Eryazici, N.C. Jeong, B.G. Hauser, C.E. Wilmer, A.A. Sarjeant, R.Q. Snurr, S.T. Nguyen, A.Ö. Yazaydin, J.T. Hupp, Metal-organic framework materials with ultrahigh surface areas: Is the sky the limit?, J. Am. Chem. Soc. 134 (2012) 15016–15021. https://doi.org/10.1021/ja3055639.

[4] I.M. Hönicke, I. Senkovska, V. Bon, I.A. Baburin, N. Bönisch, S. Raschke, J.D. Evans, S. Kaskel, Balancing Mechanical Stability and Ultrahigh Porosity in Crystalline Framework Materials, Angew. Chemie Int. Ed. 57 (2018) 13780–13783. https://doi.org/10.1002/anie.201808240.

[5] Y. He, F. Chen, B. Li, G. Qian, W. Zhou, B. Chen, Porous metal–organic frameworks for fuel storage, Coord. Chem. Rev. 373 (2018) 167–198.

https://doi.org/10.1016/j.ccr.2017.10.002.

[6] S.P. Shet, S. Shanmuga Priya, K. Sudhakar, M. Tahir, A review on current trends in potential use of metal-organic framework for hydrogen storage, Int. J. Hydrogen Energy. 46 (2021) 11782–11803. https://doi.org/10.1016/j.ijhydene.2021.01.020.

[7] W. Fan, X. Zhang, Z. Kang, X. Liu, D. Sun, Isoreticular chemistry within metal–organic frameworks for gas storage and separation, Coord. Chem. Rev. 443 (2021) 213968. https://doi.org/10.1016/j.ccr.2021.213968.

[8] A. Bavykina, N. Kolobov, I.S. Khan, J.A. Bau, A. Ramirez, J. Gascon, Metal-Organic Frameworks in Heterogeneous Catalysis: Recent Progress, New Trends, and Future Perspectives, Chem. Rev. 120 (2020) 8468–8535. https://doi.org/10.1021/acs.chemrev.9b00685.

[9] C. Xu, R. Fang, R. Luque, L. Chen, Y. Li, Functional metal–organic frameworks for catalytic applications, Coord. Chem. Rev. 388 (2019) 268–292. https://doi.org/10.1016/j.ccr.2019.03.005.

[10] A. Dhakshinamoorthy, Z. Li, H. Garcia, Catalysis and photocatalysis by metal organic frameworks, Chem. Soc. Rev. 47 (2018) 8134–8172. https://doi.org/10.1039/C8CS00256H.

[11] X. Ma, Y. Chai, P. Li, B. Wang, Metal-Organic Framework Films and Their Potential Applications in Environmental Pollution Control, Acc. Chem. Res. 52 (2019) 1461–1470. https://doi.org/10.1021/acs.accounts.9b00113.

[12] S. Rojas, A. Rodríguez-Diéguez, P. Horcajada, Metal-Organic Frameworks in Agriculture,

ACS Appl. Mater. Interfaces. 14 (2022) 16983–17007. https://doi.org/10.1021/acsami.2c00615.

[13] Y. Wen, P. Zhang, V.K. Sharma, X. Ma, H.C. Zhou, Metal-organic frameworks for environmental applications, Cell Reports Phys. Sci. 2 (2021) 100348. https://doi.org/10.1016/j.xcrp.2021.100348.

[14] L.G. Gordeeva, Y.D. Tu, Q. Pan, M.L. Palash, B.B. Saha, Y.I. Aristov, R.Z. Wang, Metal-organic frameworks for energy conversion and water harvesting: A bridge between thermal engineering and material science, Nano Energy. 84 (2021) 105946. https://doi.org/10.1016/j.nanoen.2021.105946.

[15] S. Navalón, A. Dhakshinamoorthy, M. Álvaro, B. Ferrer, H. García, Metal-Organic Frameworks as Photocatalysts for Solar-Driven Overall Water Splitting, Chem. Rev. (2022). https://doi.org/10.1021/acs.chemrev.2c00460.

[16] H. Zhang, J. Nai, L. Yu, X.W. (David) Lou, Metal-Organic-Framework-Based Materials as Platforms for Renewable Energy and Environmental Applications, Joule. 1 (2017) 77–107. https://doi.org/10.1016/j.joule.2017.08.008.

[17] C.-C. Hou, Q. Xu, Metal–Organic Frameworks for Energy, Adv. Energy Mater. 9 (2019) 1801307. https://doi.org/https://doi.org/10.1002/aenm.201801307.

[18] R.F. Mendes, F. Figueira, J.P. Leite, L. Gales, F.A. Almeida Paz, Metal–organic frameworks: a future toolbox for biomedicine?, Chem. Soc. Rev. 49 (2020) 9121–9153. https://doi.org/10.1039/D0CS00883D.

[19] P. Horcajada, R. Gref, T. Baati, P.K. Allan, G. Maurin, P. Couvreur, G. Férey, R.E. Morris, C. Serre, Metal-organic frameworks in biomedicine, Chem. Rev. 112 (2012) 1232–1268. https://doi.org/10.1021/cr200256v.

[20] X. Ma, M. Lepoitevin, C. Serre, Metal–organic frameworks towards bio-medical applications, Mater. Chem. Front. 5 (2021) 5573–5594. https://doi.org/10.1039/D1QM00784J.

[21] S. Kumar, S. Jain, M. Nehra, N. Dilbaghi, G. Marrazza, K.H. Kim, Green synthesis of metal–organic frameworks: A state-of-the-art review of potential environmental and medical applications, Coord. Chem. Rev. 420 (2020) 213407. https://doi.org/10.1016/j.ccr.2020.213407.

[22] P. Silva, S.M.F. Vilela, J.P.C. Tomé, F.A. Almeida Paz, Multifunctional metal-organic frameworks: From academia to industrial applications, Chem. Soc. Rev. 44 (2015) 6774–6803. https://doi.org/10.1039/c5cs00307e.

[23] R.G. Pearson, Hard and Soft Acids and Bases, J. Am. Chem. Soc. 85 (1963) 3533–3539. https://doi.org/10.1021/ja00905a001.

[24] K.J. Gagnon, H.P. Perry, A. Clearfield, Conventional and Unconventional Metal–Organic Frameworks Based on Phosphonate Ligands: MOFs and UMOFs, Chem. Rev. 112 (2012) 1034–1054. https://doi.org/10.1021/cr2002257.

[25] B.M. Ramesha, V. Meynen, Advances and Challenges in the Creation of Porous Metal Phosphonates, Materials (Basel). 13 (2020) 5366–5395.

[26] R.E. Yonoff, G.V. Ochoa, Y. Cardenas-Escorcia, J.I. Silva-Ortega, L. Meriño-Stand, Research trends in proton exchange membrane fuel cells during 2008–2018: A bibliometric analysis, Heliyon. 5 (2019) e01724. https://doi.org/10.1016/j.heliyon.2019.e01724.

[27] S.J. Peighambardoust, S. Rowshanzamir, M. Amjadi, Review of the proton exchange membranes for fuel cell applications, Int. J. Hydrogen Energy. 35 (2010) 9349–9384. https://doi.org/10.1016/j.ijhydene.2010.05.017.

[28] A. Kraytsberg, Y. Ein-Eli, Review of advanced materials for proton exchange membrane fuel cells, Energy Fuels. 28 (2014) 7303–7330. https://doi.org/10.1021/ef501977k.

[29] S. Shiva Kumar, V. Himabindu, Hydrogen production by PEM water electrolysis – A review, Mater. Sci. Energy Technol. 2 (2019) 442–454. https://doi.org/10.1016/j.mset.2019.03.002.

[30] A. Smoliński, N. Howaniec, Hydrogen energy, electrolyzers and fuel cells – The future of modern energy sector, Int. J. Hydrogen Energy. 45 (2020) 5607. https://doi.org/10.1016/j.ijhydene.2019.11.076.

[31] C. Van Pham, D. Escalera-López, K. Mayrhofer, S. Cherevko, S. Thiele, Essentials of High Performance Water Electrolyzers – From Catalyst Layer Materials to Electrode Engineering, Adv. Energy Mater. 11 (2021). https://doi.org/10.1002/aenm.202101998.

[32] L.L. Kang, M. Xue, Y.Y. Liu, Y.H. Yu, Y.R. Liu, G. Li, Proton conductive metal–organic frameworks based on main-group metals, Coord. Chem. Rev. 452 (2022) 214301–214338. https://doi.org/10.1016/j.ccr.2021.214301.

[33] D.W. Lim, H. Kitagawa, Rational strategies for proton-conductive metal-organic frameworks, Chem. Soc. Rev. 50 (2021) 6349–6368. https://doi.org/10.1039/d1cs00004g.

[34] H. Tang, L. Guo, X. Zheng, H. Hao, Improving proton conductivity of metal organic framework materials by reducing crystallinity, Appl. Organomet. Chem. (2022) e6777–e6790. https://doi.org/10.1002/aoc.6777.

[35] W.H. Ho, S.C. Li, Y.C. Wang, T.E. Chang, Y.T. Chiang, Y.P. Li, C.W. Kung, Proton-Conductive Cerium-Based Metal-Organic Frameworks, ACS Appl. Mater. Interfaces. 13 (2021) 55358–55366. https://doi.org/10.1021/acsami.1c17396.

[36] A. Sharma, J. Lim, S. Jeong, S. Won, J. Seong, S. Lee, Y.S. Kim, S. Bin Baek, M.S. Lah, Superprotonic Conductivity of MOF-808 Achieved by Controlling the Binding Mode of Grafted Sulfamate, Angew. Chemie - Int. Ed. 60 (2021) 14334–14338. https://doi.org/10.1002/anie.202103191.

[37] S. Wang, M. Wahiduzzaman, L. Davis, A. Tissot, W. Shepard, J. Marrot, C. Martineau-Corcos, D. Hamdane, G. Maurin, S. Devautour-Vinot, C. Serre, A robust zirconium amino acid metal-organic framework for proton conduction, Nat. Commun. 9 (2018) 1–8. https://doi.org/10.1038/s41467-018-07414-4.

[38] S.S. Bao, G.K.H. Shimizu, L.M. Zheng, Proton conductive metal phosphonate frameworks, Coord. Chem. Rev. 378 (2019) 577–594. https://doi.org/10.1016/j.ccr.2017.11.029.

[39] T. Rhauderwiek, H. Zhao, P. Hirschle, M. Döblinger, B. Bueken, H. Reinsch, D. De Vos, S. Wuttke, U. Kolb, N. Stock, Highly stable and porous porphyrin-based zirconium and hafnium phosphonates-electron crystallography as an important tool for structure

elucidation, Chem. Sci. 9 (2018) 5467–5478. https://doi.org/10.1039/c8sc01533c.

[40] T. Zheng, Z. Yang, D. Gui, Z. Liu, X. Wang, X. Dai, S. Liu, L. Zhang, Y. Gao, L. Chen, D. Sheng, Y. Wang, J. DIwu, J. Wang, R. Zhou, Z. Chai, T.E. Albrecht-Schmitt, S. Wang, Overcoming the crystallization and designability issues in the ultrastable zirconium phosphonate framework system, Nat. Commun. 8 (2017) 1–11. https://doi.org/10.1038/ncomms15369.

[41] M. Taddei, F. Costantino, F. Marmottini, A. Comotti, P. Sozzani, R. Vivani, The first route to highly stable crystalline microporous zirconium phosphonate metal–organic frameworks, Chem. Commun. 50 (2014) 14831–14834. https://doi.org/10.1039/C4CC06223J.

[42] M. Taddei, S.J.I. Shearan, A. Donnadio, M. Casciola, R. Vivani, F. Costantino, Investigating the effect of positional isomerism on the assembly of zirconium phosphonates based on tritopic linkers, Dalt. Trans. 49 (2020) 3662–3666. https://doi.org/10.1039/c9dt02463h.

[43] C.Y. Gao, J. Ai, H.R. Tian, D. Wu, Z.M. Sun, An ultrastable zirconium-phosphonate framework as bifunctional catalyst for highly active CO2 chemical transformation, Chem. Commun. 53 (2017) 1293–1296. https://doi.org/10.1039/c6cc08773f.

[44] M. Taddei, F. Costantino, R. Vivani, Synthesis and crystal structure from X-ray powder diffraction data of Two zirconium diphosphonates containing piperazine groups, Inorg. Chem. 49 (2010) 9664–9670. https://doi.org/10.1021/ic1014048.

[45] R.K. Mah, B.S. Gelfand, J.M. Taylor, G.K.H. Shimizu, Reconciling order, stability, and porosity in phosphonate metal–organic frameworks via HF-mediated synthesis, Inorg.

Chem. Front. 2 (2015) 273–277. https://doi.org/10.1039/C4QI00209A.

[46] S.M.F. Vilela, P. Salcedo-Abraira, A. Gómez-Peña, P. Trens, A. Várez, F. Salles, P. Horcajada, Proton Conductive Zr-Phosphonate UPG-1—Aminoacid Insertion as Proton Carrier Stabilizer, Molecules. 25 (2020) 3519–3535. https://doi.org/10.3390/molecules25153519.

[47] P. Salcedo-Abraira, S.M.F. Vilela, N. Ureña, F. Salles, A. Várez, P. Horcajada, Ion-Exchanged UPG-1 as Potential Electrolyte for Fuel Cells, Inorg. Chem. 60 (2021) 11803–11812. https://doi.org/10.1021/acs.inorgchem.1c00800.

[48] Y. Huang, F. Zhou, J. Feng, H. Zhao, C. Qi, J. Ji, S. Bao, T. Zheng, An ultra-stable hafnium phosphonate MOF platform for comparing the proton conductivity of various guest molecules/ions, Chem. Commun. 57 (2021) 1238–1241. https://doi.org/10.1039/d0cc07375j.

[49] M. Li, D. Li, M. O'Keeffe, O.M. Yaghi, Topological analysis of metal-organic frameworks with polytopic linkers and/or multiple building units and the minimal transitivity principle, Chem. Rev. 114 (2014) 1343–1370. https://doi.org/10.1021/cr400392k.

[50] D. Mansfeld, C. Dietz, T. Rüffer, P. Ecorchard, C. Georgi, H. Lang, M. Schürmann, K. Jurkschat, M. Mehring, Arylphosphonic acid esters as bridging ligands in coordination polymers of bismuth, Main Gr. Met. Chem. 36 (2013) 193–208. https://doi.org/10.1515/mgmc-2013-0047.

[51] P. Horcajada, P. Salcedo, S. Rojas, S.M.F. Vilela, Redes metal orgánicas a partir de pireno-fosfonato, P 201931095 ES. 2019.

[52] C. Iojoiu, P. Genova-Dimitrova, M. Maréchal, J.-Y. Sanchez, Chemical and physicochemical characterizations of ionomers, Electrochim. Acta. 51 (2006) 4789–4801. https://doi.org/https://doi.org/10.1016/j.electacta.2006.01.022.

[53] M.J. Martínez-Morlanes, A.M. Martos, A. Várez, B. Levenfeld, Synthesis and characterization of novel hybrid polysulfone/silica membranes doped with phosphomolybdic acid for fuel cell applications, J. Memb. Sci. 492 (2015) 371–379. https://doi.org/10.1016/j.memsci.2015.05.031.

[54] M.O. Cichocka, J. Ångström, B. Wang, X. Zou, S. Smeets, High-throughput continuous rotation electron diffraction data acquisition via software automation, J. Appl. Crystallogr. 51 (2018) 1652–1661. https://doi.org/10.1107/S1600576718015145.

[55] W. Kabsch, XDS, Acta Crystallogr. Sect. D Biol. Crystallogr. 66 (2010) 125–132. https://doi.org/10.1107/S0907444909047337.

[56] G.M. Sheldrick, SHELXT – Integrated space-group and crystal-structure determination, Acta Crystallogr. Sect. A Found. Adv. 71 (2015) 3–8. https://doi.org/10.1107/S2053273314026370.

[57] G.M. Sheldrick, A short history of SHELX, Acta Crystallogr. Sect. A Found. Crystallogr. 64 (2008) 112–122. https://doi.org/10.1107/S0108767307043930.

[58] M.C. Burla, R. Caliandro, B. Carrozzini, G.L. Cascarano, C. Cuocci, C. Giacovazzo, M. Mallamo, A. Mazzone, G. Polidori, Crystal structure determination and refinement via SIR2014, J. Appl. Crystallogr. 48 (2015) 306–309. https://doi.org/10.1107/S1600576715001132.

[59] V.A. Blatov, A.P. Shevchenko, D.M. Proserpio, Applied Topological Analysis of Crystal Structures with the Program Package ToposPro, Cryst. Growth Des. 14 (2014) 3576–3586. https://doi.org/10.1021/cg500498k.

[60] O. Delgado-Friedrichs, M. O'Keeffe, Identification of and symmetry computation for crystal nets, Acta Crystallogr. Sect. A Found. Crystallogr. 59 (2003) 351–360. https://doi.org/10.1107/S0108767303012017.

[61] O. Delgado-Friedrichs, The Gavrog Project, (2017) http://gavrog.org/.

[62] J. Rodríguez-Carvajal, Recent advances in magnetic structure determination by neutron powder diffraction, Phys. B Condens. Matter. 192 (1993) 55–69. https://doi.org/10.1016/0921-4526(93)90108-I.

[63] A.K. Rappe, C.J. Casewit, K.S. Colwell, W.A. Goddard, W.M. Skiff, UFF, a full periodic table force field for molecular mechanics and molecular dynamics simulations, J. Am. Chem. Soc. 114 (1992) 10024–10035. https://doi.org/10.1021/ja00051a040.

[64] T. Düren, F. Millange, G. Férey, K.S. Walton, R.Q. Snurr, Calculating Geometric Surface Areas as a Characterization Tool for Metal−Organic Frameworks, J. Phys. Chem. C. 111 (2007) 15350–15356. https://doi.org/10.1021/jp074723h.

[65] L.D. Gelb, K.E. Gubbins, Pore Size Distributions in Porous Glasses: A Computer Simulation Study, Langmuir. 15 (1999) 305–308. https://doi.org/10.1021/la9808418.

[66] V.U. Zview 2 for Windows (Version 2.0), Scribner Assoc. Inc., Zview 2 for Windows (Version 2.0). Scribner Assoc. Inc., VA USA (2000), (2000).

[67] N. Stock, High-throughput investigations employing solvothermal syntheses, Microporous Mesoporous Mater. 129 (2010) 287–295. https://doi.org/10.1016/j.micromeso.2009.06.007.

[68] Z. Huang, E.S. Grape, J. Li, A.K. Inge, X. Zou, 3D electron diffraction as an important technique for structure elucidation of metal-organic frameworks and covalent organic frameworks, Coord. Chem. Rev. 427 (2021) 213583–213597. https://doi.org/https://doi.org/10.1016/j.ccr.2020.213583.

[69] G.S. Fulcher, Analysis of Recent Measurements of the Viscosity of Glasses, J. Am. Ceram. Soc. 75 (1992) 1043–1055. https://doi.org/10.1111/j.1151-2916.1992.tb05536.x.

[70] K.M. Diederichsen, H.G. Buss, B.D. McCloskey, The Compensation Effect in the Vogel-Tammann-Fulcher (VTF) Equation for Polymer-Based Electrolytes, Macromolecules. 50 (2017) 3831–3840. https://doi.org/10.1021/acs.macromol.7b00423.

[71] T. Ogawa, T. Aonuma, T. Tamaki, H. Ohashi, H. Ushiyama, K. Yamashita, T. Yamaguchi, The proton conduction mechanism in a material consisting of packed acids, Chem. Sci. 5 (2014) 4878–4887. https://doi.org/10.1039/c4sc00952e.

[72] Y. Gao, R. Broersen, W. Hageman, N. Yan, M.C. Mittelmeijer-Hazeleger, G. Rothenberg, S. Tanase, High proton conductivity in cyanide-bridged metal-organic frameworks: understanding the role of water, J. Mater. Chem. A. 3 (2015) 22347–22352. https://doi.org/10.1039/c5ta05280g.

[73] C.J.T. de Grotthuss, Memoir on the decomposition of water and of the bodies that it holds in solution by means of galvanic electricity, Biochim. Biophys. Acta - Bioenerg. 1757

(2006) 871–875. https://doi.org/10.1016/j.bbabio.2006.07.004.

[74] H.R. Allcock, M.V.B. Phelps, E.W. Barrett, M. V. Pishko, W.G. Koh, Ultraviolet photolithographic development of polyphosphazene hydrogel microstructures for potential use in microarray biosensors, Chem. Mater. 18 (2006) 609–613. https://doi.org/10.1021/cm050316b.

[75] A.M. Martos, J.-Y. Sanchez, A. Várez, B. Levenfeld, Electrochemical and structural characterization of sulfonated polysulfone, Polym. Test. 45 (2015) 185–193. https://doi.org/https://doi.org/10.1016/j.polymertesting.2015.06.004.

[76] S.M.F. Vilela, J.A.R. Navarro, P. Barbosa, R.F. Mendes, G. Pérez-Sánchez, H. Nowell, D. Ananias, F. Figueiredo, J.R.B. Gomes, J.P.C. Tomé, F.A.A. Paz, Multifunctionality in an Ion-Exchanged Porous Metal–Organic Framework, J. Am. Chem. Soc. 143 (2021) 1365–1376. https://doi.org/10.1021/jacs.0c10421.

[77] S.M. Elahi, S. Chand, W. Deng, A. Pal, M.C. Das, Polycarboxylate-Templated Coordination Polymers: Role of Templates for Superprotonic Conductivities of up to 10 −1 S cm −1, Angew. Chemie Int. Ed. 57 (2018) 6662–6666. https://doi.org/10.1002/anie.201802632.

[78] F. Yang, G. Xu, Y. Dou, B. Wang, H. Zhang, H. Wu, W. Zhou, J.-R. Li, B. Chen, A flexible metal–organic framework with a high density of sulfonic acid sites for proton conduction, Nat. Energy. 2 (2017) 877–883. https://doi.org/10.1038/s41560-017-0018-7.